buildings

MDPI

Article

Experimental and Numerical Simulation Study on the Mechanical Properties of Integrated Sleeve Mortise and Tenon Steel–Wood Composite Joints

Zhanguang Wang [1,2], Weihan Yang [3], Zhenyu Gao [2], Jianhua Shao [2,*] and Dongmei Li [2]

[1] School of Architectural Engineering, Kaili University, Kaili 556011, China; wzg3262396@163.com
[2] School of Civil Engineering and Architecture, Jiangsu University of Science and Technology, Zhenjiang 212003, China; 85565118@163.com (Z.G.); 18484417527@163.com (D.L.)
[3] School of Civil and Architectural Engineering, Nanchang Institute of Technology, Nanchang 330099, China
* Correspondence: shaojianhua97@163.com

Abstract: In view of the application status and technical challenges of steel–wood composite joints in architecture, this paper proposes an innovative connection technology to solve issues such as susceptibility to pry-out at beam–column joints and low load-bearing capacity and to provide various reinforcement methods in order to meet the different structural requirements and economic benefits. By designing and manufacturing four groups of beam–column joint specimens with different reinforcement methods, including no reinforcement, structural adhesive and angle steel reinforcement, 4 mm thick steel sleeve reinforcement, and 6 mm thick steel sleeve reinforcement, monotonic loading tests and finite element simulations were carried out, respectively. This research found that unreinforced specimens and structural adhesive angle steel-reinforced joints exhibited obvious mortise and tenon compression deformation and, moreover, tenon pulling phenomena at load values of approximately 2 kN and 2.6 kN, respectively. However, the joint reinforced by a steel sleeve showed a significant improvement in the tenon pulling phenomenon and demonstrated excellent initial stiffness characteristics. The failure mode of the steel sleeve-reinforced joints is primarily characterized by the propagation of cracks at the edges of the steel plate and the tearing of the wood, but the overall structure remains intact. The initial rotational stiffness of the joints reinforced with angle steel and self-tapping screws, the joints reinforced with 4 mm thick steel sleeves, and the joints reinforced with 6 mm thick steel sleeves are 3.96, 6.99, and 13.62 times that of the pure wooden joints, while the ultimate bending moments are 1.97, 7.11, and 7.39 times, respectively. Using finite element software to simulate four groups of joints to observe their stress changes, the areas with high stress in the joints without sleeve reinforcement are mainly located at the upper and lower ends of the tenon, where the compressive stress at the upper edge of the tenon and the tensile stress at the lower flange are both distributed along the grain direction of the beam. The stress on the column sleeve of the joints reinforced with steel sleeves and bolts is relatively low, while the areas with high strain in the beam sleeve are mainly concentrated on the side with the welded stiffeners and its surroundings; the strain around the bolt holes is also quite noticeable.

Keywords: steel–wood composite joint; reinforcement technology; monotonic loading test; bearing capacity; M–θ relationship

Academic Editor: Paulo Santos

Received: 5 December 2024
Revised: 28 December 2024
Accepted: 29 December 2024
Published: 4 January 2025

Citation: Wang, Z.; Yang, W.; Gao, Z.; Shao, J.; Li, D. Experimental and Numerical Simulation Study on the Mechanical Properties of Integrated Sleeve Mortise and Tenon Steel–Wood Composite Joints. *Buildings* **2025**, *15*, 137. https://doi.org/10.3390/buildings15010137

1. Introduction

In the long history of China, the ancient wooden architecture system is unique and has become an important part of historical culture. At present, a large number of traditional ethnic wooden structures are still preserved in the southwest region, showing their cultural charm. Wood, as a renewable material, has the advantages of light weight, non-toxicity, and easy processing, which is in line with the concepts of sustainable development and green architecture. However, the mechanical properties of wood are anisotropic, especially the insufficient compressive performance in the longitudinal direction, which affects the safety and stability of the structure. The defects of wood are effectively compensated by steel with the advantages of high strength, isotropy, ease of construction, strong plasticity, and good seismic performance. Therefore, the combination of wood and steel can provide full play to the advantages of the two materials and achieve complementary effects. Domestic and foreign scholars have conducted in-depth research on modern steel–wood composite joints, including mortise and tenon connections, metal fittings connections, and rebar connections, aiming to achieve complementary advantages of materials and promote the innovation and development of construction technology.

In the research of mortise and tenon connections, Fa Guanzhe et al. reinforced mortise and tenon joints in timber structures with BFRP (basalt fiber reinforced polymer) and concluded that the load-bearing capacity and stiffness of the joints were significantly improved after reinforcement [1]. Zhou Qian et al. used steel members for reinforcement, reducing the amount of tenon pulling and enhancing the flexural bearing capacity and energy dissipation ability [2]. Xu Minggang et al. proposed the carbon fiber cloth reinforcement method, effectively enhancing the seismic performance [3]. Mortise and tenon joints in the Taiwan region were subjected to monotonic loading tests by Chang et al. [4,5], who studied the effects of different initial gaps on the bending stiffness of the joints. The seismic performance of steel plate shear walls was studied by Shao Jianhua et al. [6–12], who conducted experimental research on the seismic performance of the system and concluded that the energy absorption capacity of the shear walls was significantly enhanced after reinforcement. Chen Chunchao et al. studied the failure modes of asymmetric mortise and tenon joints and clarified their mechanical properties [13]. Yang Huifeng et al. reinforced the joints using the bar embedding method and conducted relevant experiments, concluding that the ultimate load-bearing capacity and ductility of the reinforced joints were significantly improved [14]. Thomas Tannert et al. designed various reinforcement methods for the dovetail mortise and tenon joints and conducted pseudo-static tests, concluding that the connection stiffness of the reinforced joints was significantly improved [15]. Emile Crayssac et al. studied the enhancement of the seismic resistance of mortise and tenon frames by panel filling [16]. Aryan Rezaei Rad et al. analyzed the force-deformation response of through-tenon connections and pointed out their low ductility characteristics [17]. Lydia Panoutsopoulou et al. revealed the relationship between the bearing capacity and stress state of mortise–tenon T-joints through loading tests [18].

In the research of metal fittings connections, Wang Mingqian et al. studied the rotational deformation ability of bolt–steel filler plate joints through tests and simulations and pointed out the influence of bolt diameter on stiffness [19]. Sun Hongfeng et al. studied the bearing capacity of beam–column joints after self-tapping screw reinforcement and proposed a theoretical calculation method [20]. Luo Erhu optimized the bolted joints of timber structures filled with steel plates and conducted low-cycle repeated loading tests, concluding that the bending stiffness and load-bearing capacity of the optimized joints were significantly improved [21]. Zhou T et al. used three-dimensional finite element simulation to predict the dowel bearing strength and verified the accuracy of the model [22]. Thomas K B et al. analyzed the stress changes of bolted joints with internal steel plates and verified

the European yield theory [23]. Mahyar Masaeli et al. studied the influence of different bolt arrangements on the performance of LVL double-beam to column connectors and established an interaction model [24].

Therefore, based on the existing research results, this paper designs a new type of integrated sleeve mortise and tenon steel–wood composite beam–column joint to address issues, such as the susceptibility to pry-out at beam–column joints and low load-bearing capacity, and to provide various reinforcement methods that cater to different structural requirements and economic benefits. Through the monotonic loading test of the integrated sleeve mortise and tenon steel–wood composite beam–column joint, the influence of various situations such as no reinforcement, structural adhesive and angle steel reinforcement, 4 mm thick steel sleeve reinforcement, and 6 mm thick steel sleeve reinforcement on the mechanical properties of the steel–wood composite beam–column joint is analyzed.

2. Experimental Study

2.1. Specimen Design and Fabrication

The new integrated sleeve mortise and tenon steel–wood composite beam–column joint is a new type of composite joint that is prefabricated and assembled on site. The wooden beams, wooden columns, and steel sleeves are prefabricated in the factory and can be conveniently fixed on the construction site with just bolt connections. In this study, six beam–column joints were selected as test objects, and the reinforcement method was taken as the main parameter, which was divided into no reinforcement, structural adhesive and angle steel reinforcement, 4 mm thick steel sleeve reinforcement, and other forms, and monotonic loading tests were carried out on them. Based on the test results, the specific influence of various reinforcement methods on the mechanical properties and failure modes of the joints was analyzed. This study follows the principle of "strong column and weak beam". According to the practice in "Yingzao Fashi" [25], four joints were fabricated with a scale reduction of 1:3.25, and these specimens are numbered from J-1 to J-4. The comparison of the reinforcement methods of each joint is shown in Table 1.

Table 1. Basic parameters of specimens.

Specimen Number	Reinforcement Method	Steel Plate Thickness/mm
J-1	None	-
J-2	Structural adhesive, angle steel, self-tapping screw	4
J-3	Steel sleeve	4
J-4	Steel sleeve	6

The length of the wooden column in each joint was set to 800 mm in the monotonic loading test, the cross-sectional dimension was 150 × 150 mm, and it was cut along the center line of the column. The depth of the mortise hole was set to 75 mm. At the same time, the length of the beam was set to 600 mm, the cross-sectional dimension was 100 × 150 mm, and a tenon-like protrusion was set at the beam end, with a depth of 75 mm and a cross-sectional dimension of 50 × 150 mm. The main variable under the monotonic loading test was the reinforcement method, while the J-1 joint was a pure wooden structure, and no structural adhesive was added between the tenon and the mortise hole. The J-2 joint reinforced the side of the joint area with structural adhesive and self-tapping screws, and angle steels were attached to both sides of the upper and lower flanges of the joint area and fixed to the wooden column and wooden beam with self-tapping screws. As for the J-3 and J-4 joints, the specimens included components such as wooden beams, wooden columns, four column–beam steel sleeves, stiffening ribs, and high-strength bolts. Bolt

holes were reserved during the manufacturing process. The joint core area of the column sleeve was welded to the outer extension end plate on the beam sleeve, and stiffening ribs were pre-welded on the upper and lower surfaces of the beam sleeve. Finally, the beam–column and beam–column steel sleeves were bound into a whole by high-strength bolts passing through the reserved bolt holes. The schematic diagrams of each joint are shown in Figure 1.

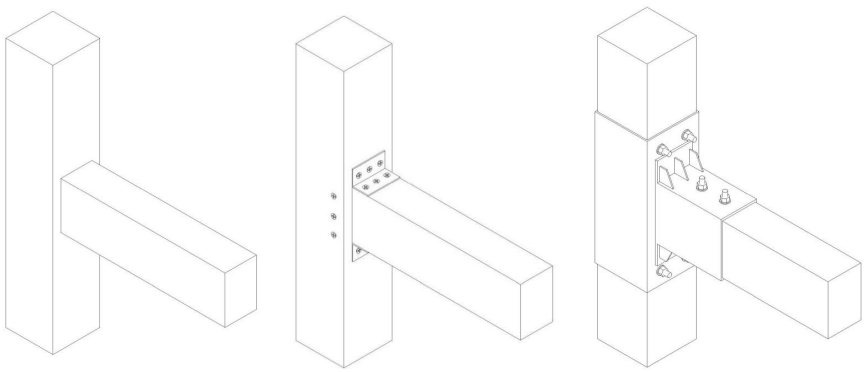

(**a**) (**b**) (**c**)

Figure 1. Nodes J-1 to J-4. (**a**) J-1, (**b**) J-2, and (**c**) J-3 and J-4.

In the specimen J-2, six self-tapping screws with a diameter of 3 mm and a length of 60 mm were used, the thickness of the angle steel was 3 mm, the height and width were both 50 mm, and the length was 100 mm. In addition, 12 self-tapping screws of the same specification were used to firmly fix the angle steel. The steel–wood composite joints J-3 and J-4 are illustrated in Figure 2. Taking the J-3 joint as an example, the beam and column steel sleeves are both composed of 4 mm thick Q235 steel, and the stiffening ribs are composed of 3 mm steel. The column sleeve with the cross-sectional dimension of 158 × 158 mm is composed of a vertical sleeve. The beam sleeve includes an outer extension plate, a sleeve, and stiffening ribs. The outer extension plate has a cross-section of 108 × 278 mm, the length of the sleeve is 200 mm, and the cross-sectional dimension is 108 × 158 mm. The dimensions prefabricated in the factory are relatively accurate. Therefore, the diameter of the holes reserved for the beam–column and beam–column sleeve is set to 13 mm, and 6 high-strength bolts of grade 10.9 M12 are selected as bolts. The beam and column steel sleeves of the J-4 joint are both composed of 6 mm thick Q235 steel, and the other structures are the same as those of the J-3 joint.

2.2. Test Loading

This test adopts a monotonic load test. A 10-ton hydraulic jack manufactured by Shanghai Tali Machinery Co., Ltd. (Shanghai, China) is used to apply a vertical load to the top of the column; the load is set to 25 kN, and the value is monitored by a pressure sensor. In order to accurately simulate the hinged state, the top of the column is fixedly connected to the side wall of the reaction frame by four clamps and four M15 bolts, and the bottom is fixedly connected to the ground by two clamps and four M15 bolts. A 20-ton hydraulic jack manufactured by Shanghai Tali Machinery Co., Ltd. is used to apply a one-way load at the beam end, and the value for the jacks is also monitored by a pressure sensor. The test was carried out in the heavy-duty laboratory of Jiangsu University of Science and Technology, and the three-dimensional view of the loading equipment is shown in Figure 3. A load-controlled loading system is adopted at the beam end. The amplitude of the first loading is set to 0.1 kN, and this load is used as the reference for subsequent loadings, with

the load being increased by 0.1 kN each time, until the structure is damaged, as plotted in Figure 4.

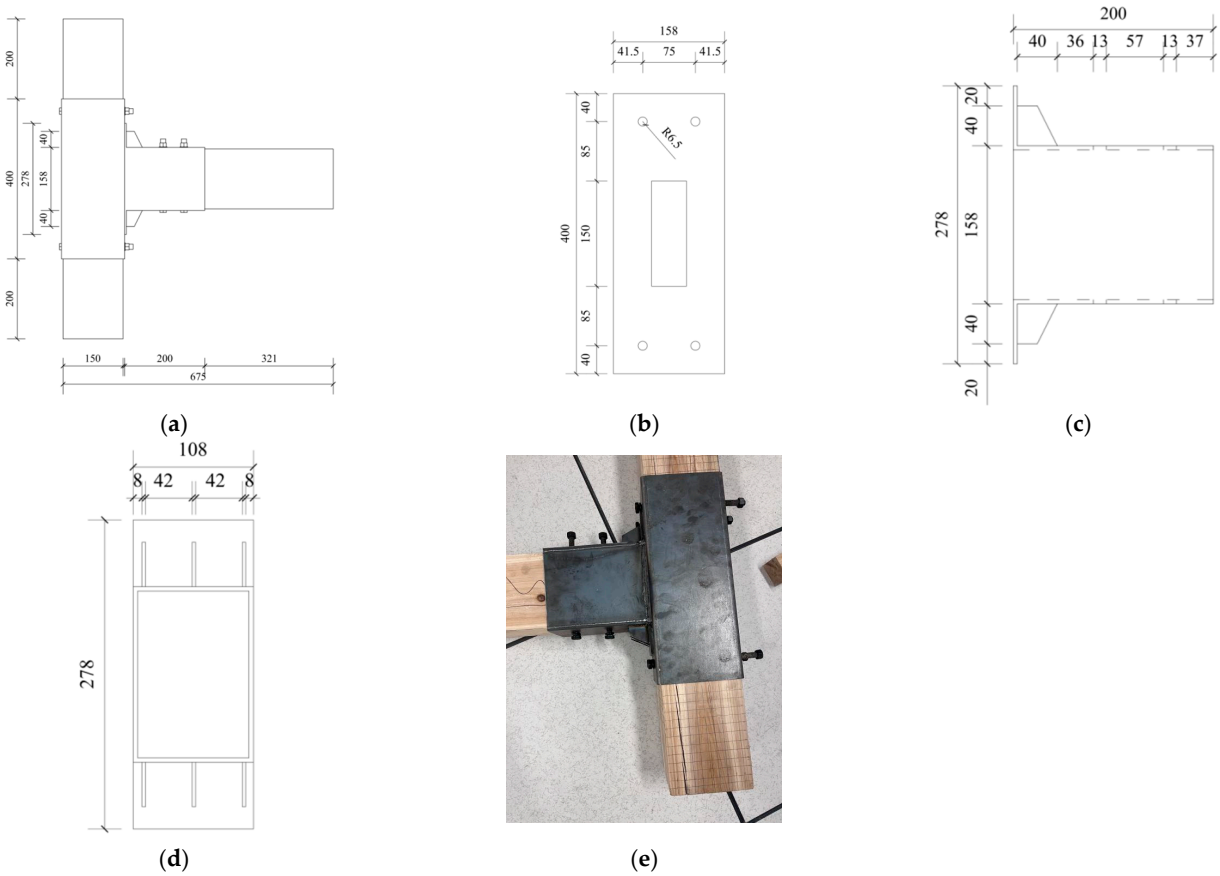

Figure 2. Design drawings of node J-3 and node J-4. (**a**) Left view of the steel sleeve of the column, (**b**) front view of the steel sleeve of the column, (**c**) left view of the steel sleeve of the beam, and (**d**) front view of the steel sleeve of the beam. (**e**) Completed node assembly diagram.

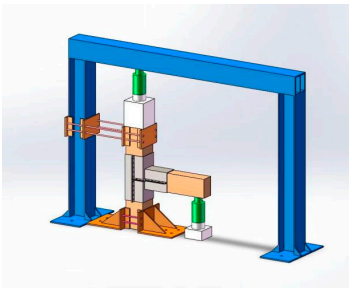

Figure 3. Three-dimensional view of the loading device.

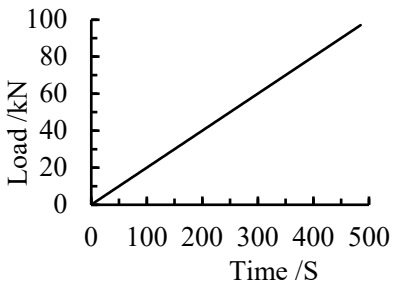

Figure 4. Loading regime.

2.3. Measuring Point Arrangement and Measuring Point Content

The strain gauge model BFH120-3AA-X30 is selected for use in the monotonic loading test, and the strain measuring devices are pasted on the upper and lower surfaces where the supporting wooden beam contacts the steel sleeve, the left and right surfaces where the wooden column contacts the column sleeve, and the surfaces of the upper and lower stiffening ribs. The detailed arrangement of the strain measuring points of each joint is shown in Figure 5.

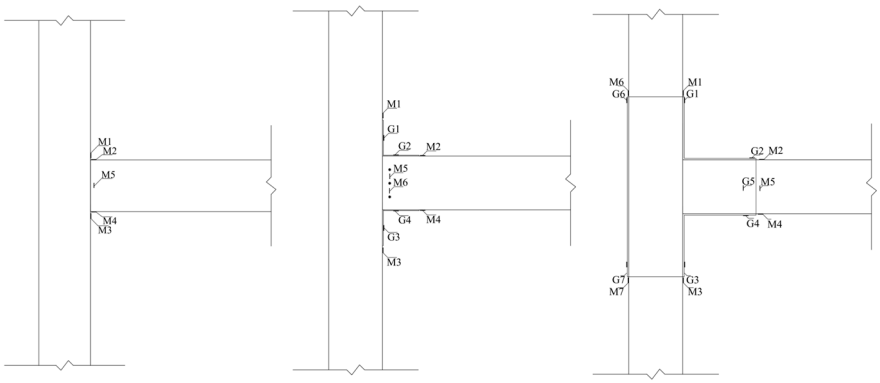

(**a**) (**b**) (**c**)

Figure 5. Layout drawing of measuring points. (**a**) J-1, (**b**) J-2, and (**c**) J-3 and J-4.

Five displacement meters are used to measure the displacement of the joint. The bases of the displacement meters D1, D2, and D3 are closely attached to the adjacent H-section steel, and the measuring rods of the displacement meters are all parallel to the axis of the beam. The contacts are closely attached to the surface of the beam slab, and the value is ensured to be stable at −50 mm. The displacement meter, located 460 mm away from column D1 and above the midline of the beam, is used to measure the vertical displacement of the beam end, as shown in Figure 6a. Displacement meters D2 and D3, symmetrically arranged on both sides of the midline of beam at distances of 30 mm from the midline of beam and 230 mm from the column, are used to detect whether the beam undergoes torsional deformation under monotonic loading and to verify the accuracy of the values from displacement meter D1. On the other hand, the displacement meters D4 and D5 are installed on the midline of the column, symmetrically distributed in the upper and lower 1/8 column length regions of the center of the column, and used to measure the rotational angular displacement of the column during the loading process, as plotted in Figure 6b.

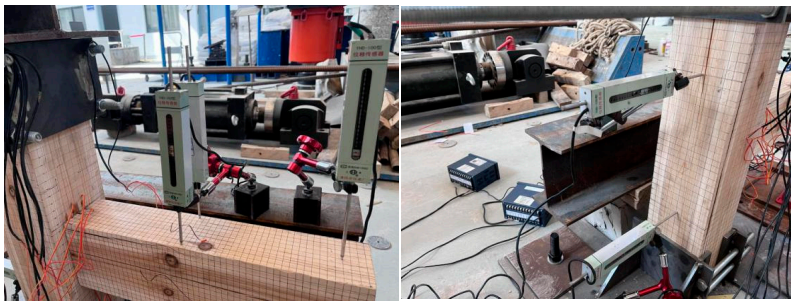

(**a**) (**b**)

Figure 6. Distribution diagram of displacement meters. (**a**) D1, D2, and D3; (**b**) D4 and D5.

3. Experimental Result Analysis

3.1. Joint Failure Phenomenon

During the loading process of the joint, when the load cannot be further applied and the specimen undergoes significant deformation, it can be considered that the joint has been damaged, and the test stops loading. The load at this point is the maximum load-bearing capacity of the joint, which can also be represented as the critical value.

3.1.1. Failure Phenomenon of Specimen J-1

The loading schematic diagram of the J-1 joint is shown in Figure 7a. A slight creaking sound appeared in the structure when the load reached the first level of 0.1 kN. With the continuous increase in the load, the creaking sound became more and more obvious, and cracks appeared between the tenon and the mortise hole. When the load reached 0.28 kN, it could be observed that the lower flange of the tenon of the beam had partially separated from the mortise hole, as shown in Figure 7b. The pulling-out amount of the lower end of the tenon had reached 2.5 cm when the load increased to 0.4 kN, and when the load was increased from 0.5 kN to 0.68 kN, with the creaking sound in the structure, a short unloading phenomenon occurred, and the upper flange of the tenon showed a significant extrusion deformation. The unloading phenomenon became remarkably obvious with the further increase in the load, and the load fluctuated repeatedly between 0.7 kN and 0.88 kN. Considering that the deformation of the structure was quite obvious and that the load could not be continued to be increased, it was determined that the test was terminated, and the deformation of the joint is shown in Figure 7c.

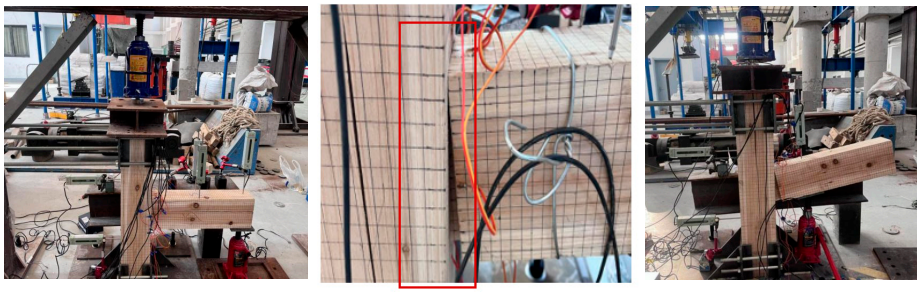

(**a**) (**b**) (**c**)

Figure 7. Deformation diagram of node J-1. (**a**) Overall view before the test, (**b**) tenon pulling diagram of the lower flange of the beam, and (**c**) deformation diagram of the specimen after failure.

3.1.2. Failure Phenomenon of Specimen J-2

The initial stiffness of the J-2 joint was increased compared with that of the J-1 joint in the initial stage of load application. After that, when the load continued to increase to 0.6 kN, a slight abnormal sound appeared in the structure, and a slight pulling-out seam appeared at the lower flange of the tenon. The abnormal sound became more and more dense with the further increase in the load, as illustrated in Figure 8a, and the self-tapping screws were partially pulled out as the displacement increased. Until the load reached 1.0 kN, an obvious crack appeared along the axial direction of the wooden beam, the self-tapping screws connecting the angle steel and the wooden column were pulled out when the load increased to 1.7 kN, and the width of the pulling-out seam had reached 2.5 cm, as shown in Figure 8b. A repeated unloading phenomenon began to appear in the structure when the load increased to 3.0 kN, and the displacement change of the wooden beam was particularly significant; the test loading was ended.

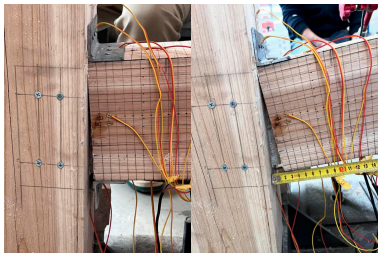

(**a**) (**b**)

Figure 8. Deformation diagram of node J-2. (**a**) Deformation diagram with an increased degree of tenon pulling and (**b**) deformation diagram with a tenon pulling amount of 2.5 cm.

3.1.3. Failure Phenomenon of Specimen J-3

The upper and lower flange wall thicknesses of the beam steel sleeve of the specimen J-3 are both 4 mm, the sleeve length is 200 mm, and the bolt spacing needs to meet the requirement of 1.5d specified in the Code for Design of Timber Structures [17]. By opening holes in the wooden beam and the steel sleeve, six high-strength bolts of grade M10.9 are used for connection.

Due to the need to reserve a 1–2 mm gap between the tenon and the mortise hole and between the beam sleeve and the wooden beam in the actual production process, the existence of these gaps makes the structure slide to a certain extent in the initial loading stage. The gap between the upper surface of the wooden beam and the upper flange of the beam sleeve gradually decreases with the increase in the load. A short popping sound appears in the structure, and there is no obvious visible crack when the load reaches 4.8 kN. However, an obvious creaking sound appears again in the structure when the load increases to 5.8 kN. With the further increase in the load, the displacement of the wooden beam gradually increases, and the creaking sound becomes closer. When the load reaches 8.8 kN, it can be observed that a crack appears along the axial direction in the middle of the wooden beam and that the upper surface of the wooden beam shows obvious compressive deformation. When the load increases to 12.4 kN, it can be observed that the vertical axial force at the column end increases to twice the initially applied axial force at this time, and the inclination of the beam is significant, as shown in Figure 9a. When the load reaches 17.4 kN, cracks appear on the wooden column, and an obvious tearing sound appears on the wooden beam, the upper surface of the beam sleeve gradually shows obvious bulging, and there is an obvious bulge at the stiffening rib. When the load increases to 31.4 kN, as shown in Figure 9b,c, the upper flange of the beam sleeve is squeezed to the edge and broken, the lower flange is distorted into a W shape, and the axial force at the column end increases to 80 kN. Considering that the deformation of the steel plate is too large and the unloading phenomenon has occurred continuously during the loading process, this result determined that the specimen has failed, and the test was stopped.

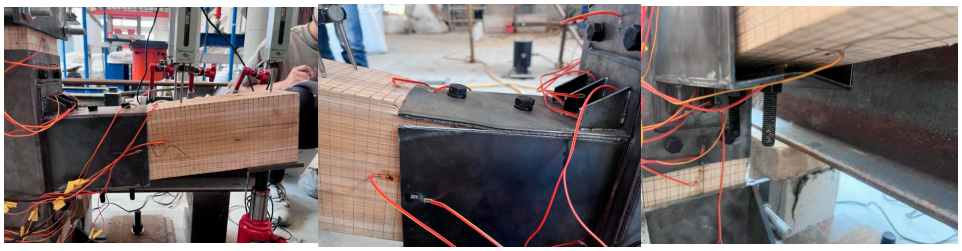

(**a**) (**b**) (**c**)

Figure 9. Deformation diagram of node J-3. (**a**) Deformation diagram of the wooden beam under extrusion and tilting, (**b**) deformation diagram of the edge fracture of the upper flange, and (**c**) deformation diagram of the extrusion of the lower flange.

3.1.4. Failure Phenomenon of Specimen J-4

The main difference between specimen J-4 and J-3 lies in that the thickness of the upper and lower flanges of the beam steel sleeve and the extended end plate is 6 mm and that its bolt spacing also meets the requirement of 1.5d.

During the initial loading stage, specimen J-4 also exhibited a certain degree of initial sliding due to the 1–2 mm gap reserved between the tenon and mortise hole in actual production and the clearance between the beam sleeve and the wooden beam. As the load increased, the gap between the upper surface of the wooden beam and the upper flange of the beam sleeve further narrowed. When the load increased to 4.3 kN, a brief squeaking sound occurred in the structure, and the upper flange of the wooden beam showed a slight extrusion deformation, but no obvious cracks were found; meanwhile, the gap between the lower flange of the wooden beam and the sleeve became more significant, as shown in Figure 10a. When the load increased to 6 kN, an obvious squeaking sound occurred again in the structure, and the upper surface of the wooden beam showed significant extrusion damage and was embedded into the beam sleeve. When the load increased to 13.2 kN, a crack could be seen along the axis in the middle of the wooden beam, and a continuous tearing sound occurred in the structure. It could be observed that the inclination of the beam was relatively large, and the upper flange of the beam sleeve was extruded to the extent that cracks appeared, as shown in Figure 10b. When the load increased to 33 kN, the squeaking and cracking sound was very sharp and loud, and the upper surface of the wooden beam was broken, with obvious debris, as shown in Figure 10c. At this time, the axial force at the column end rose to 65 kN. Considering that the steel plate was excessively deformed and that there was a continuous unloading phenomenon during the loading process, it was judged that the specimen had been damaged.

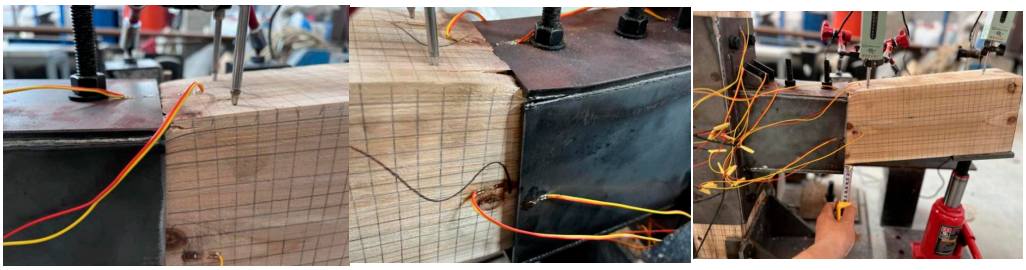

(**a**) (**b**) (**c**)

Figure 10. Deformation diagram of the J-4 joint. (**a**) Squeezing deformation diagram of the upper flange, (**b**) fracture diagram of the upper flange of the wooden beam and the steel plate, and (**c**) deformation diagram of the wooden beam.

By comparing and analyzing the test results of joints J-1, J-2, J-3, and J-4, it can be seen that both the J-1 and J-2 components were not suitable for bearing large loads due to different degrees of slippage of the tenon. After introducing structural glue, self-tapping screws, and angle steel into the pure wood joint, the flexural and shear capacities, stiffness, and ultimate bearing capacity of the joint would be correspondingly improved. The sleeve-strengthened J-3 and J-4 joints all failed at the beam end lap joint. In comparison, the degree of damage at the beam end was more significant than that of specimen J-3 due to the increased wall thickness of the beam sleeve of specimen J-4, while the steel plate did not show obvious bulging deformation. However, from the perspective of the entire structural system, both the initial stiffness and the ultimate bearing capacity of the joints were improved to a certain extent. At the same time, by observing the change in the axial force at the column end during the test of specimens J-3 and J-4, it was found that the growth rate of the axial force at the column end of specimen J-3 was greater than that of

specimen J-4. This was mainly because the thickness of the steel plate at the upper and lower flanges of the beam sleeve of specimen J-4 was increased, and its flexural and shear properties were enhanced, thereby reducing the bending moment acting on the column body transferred by the load.

The tenon pulling-out failure is the most common damage mode in ancient wooden buildings. Among all of the joints, the tenon pulling-out amount of joint J-1 was the largest, reaching 30 mm, and that of joint J-2 was 3 mm. In joints J-3 and J-4, the bolt connection between the sleeve and the wooden beam avoided the tenon pulling-out phenomenon, and the tenon pulling-out amount was extremely small.

3.2. Analysis of the Results of the Node Moment—Rotation Curve

By sorting and analyzing the test loading load and joint displacement, the moment–rotation (M–θ) curves of each joint can be obtained, as shown in Figure 11.

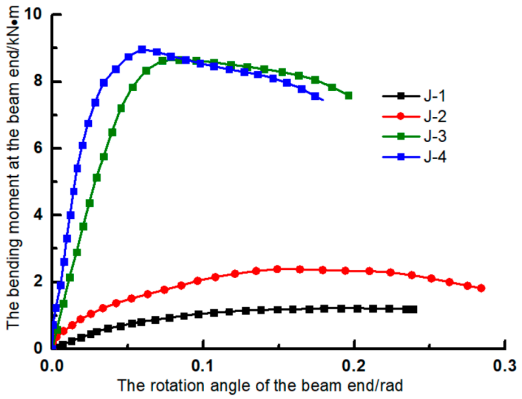

Figure 11. Comparison of the node moment—rotation curves.

As can be seen from Figure 11, the M–θ curves of the J-1~J-4 joints without sleeve reinforcement have the following characteristics:

(1) Each joint change is divided into elastic, yielding, strengthening, and descending stages, and the curve shows a trend of rising–flattening–descending. The deformation and stress of the mortise–tenon interface increase during the initial loading stage, and the M–θ curve grows linearly in the elastic stage. As the bending moment increases, the yielding deformation of the mortise–tenon increases, and the curve stiffness decreases with the appearance of a platform in the yielding stage. After the joint yields, it enters the strengthening stage, the stress of the tenon increases excessively, and the joint has plastic deformation, with the upper surface of the tenon being extruded and the lower surface being stretched. As the plastic deformation increases, the contact area between the lower surface of the tenon and the mortise hole decreases, and the unloading curve of the joint enters the descending stage until the end of the test.

(2) Comparing the M–θ curves of joints J-1 and J-2, with the increase in reinforcement methods, the initial stiffness and ultimate bending moment of each joint are significantly improved. Comparing joints J-2 and J-1, the angle steel restricts the beam end displacement during the initial loading stage, making the initial stiffness of J-2 greater than that of J-1. As the self-tapping screws are pulled out, the J-2 curve enters the yielding, rising, and strengthening stages. At this time, the lower angle steel connection column end screws fail, and the ultimate bending moment value of J-2 is greater than that of J-1. In the descending section of the curve, due to the resistance of the upper angle steel to the bending moment, the lower surface of the tenon detaches from the mortise opening faster, and the curve descends more rapidly.

(3) For the sleeve-reinforced J-3 and J-4 joints, their strength and stiffness are significantly improved compared with J-1 and J-2. Although there are differences in the curve changes of the two joints, the overall trend is consistent. Compared with the joints without sleeve reinforcement, there is a significant difference in the rising stage of the curve. During the initial loading stage, the steel sleeve and the through bolts restrict the displacement of the wooden beam, and the rotational stiffness of the structure rises along the Y-axis, making the joint nearly rigid. With the plastic deformation of the bolt holes of the wooden beam and the lap joint of the sleeve and the bending deformation of the sleeve, after the joint enters the yielding stage, there is a strengthening stage, and the stiffness slowly rises with the increase in the load until the ultimate bending moment. Then, the curve enters the descending stage due to the damage of the steel plate and the cracking of the wooden beam.

(4) The initial rotational stiffness of J-2, J-3, and J-4 are 3.96, 6.99, and 13.62 times that of J-1, while the ultimate bending moments are 1.97, 7.11, and 7.39 times, respectively.

The main mechanical performance parameters related to the specimen joints J-1–J-4 are shown in Table 2.

Table 2. Mechanical performance parameters of the sleeve-reinforced joints.

Specimen Number	Initial Rotational Stiffness/(kN·m/rad)	Yielding Bending Moment/(kN·m)	Ultimate Bending Moment/(kN·m)
J-1	25.03	0.901	1.214
J-2	99	1.84	2.392
J-3	175	7.176	8.625
J-4	341	8.418	8.97

4. Finite Element Numerical Simulation and Verification

In this paper, the finite element analysis software ABAQUS2021 was used to numerically simulate the joints.

4.1. Constitutive Relationship of Materials

4.1.1. Constitutive Relationship of Wood Along the Grain

The test material is Chinese fir, which belongs to orthotropic materials. For the convenience of calculation, the compressive and tensile capacities of wood along the grain are both regarded as an ideal elastoplastic model, and the elastic modulus of wood with respect to compression along the grain is equal to that of tension along the grain. As shown in Figure 12, the stress–strain relationship of wood in compression along the grain is reflected in a bilinear model, while the stress–strain curve of wood in tension along the grain adopts a single-line model [26].

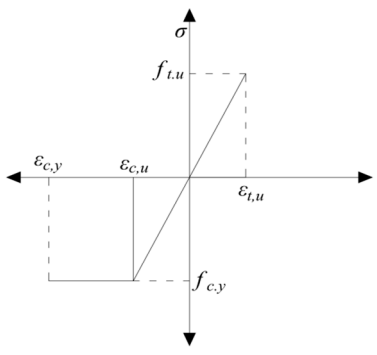

Figure 12. Constitutive model of wood in terms of compression and tension along the grain.

4.1.2. Constitutive Relationship of Wood Across the Grain

During the calculation process, the transverse grain of wood undergoes large plastic deformations when compressed, which makes it difficult to determine the final failure point of the wood, and the stress increment in the strengthening phase is limited. Therefore, the stress–strain curve of wood under transverse compression is typically simplified to the bilinear model shown in Figure 13 [27].

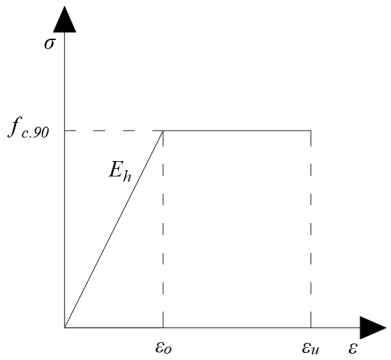

Figure 13. Constitutive model of wood in terms of compression across the grain.

In ABAQUS software, following the traditional definition of wood, its three material directions are defined, namely the longitudinal direction (L), the radial direction across the grain (R), and the tangential direction across the grain (T) [28]. Engineering constants are widely used to describe the anisotropic elastic properties of wood, with a total of nine independent parameters, including elastic moduli (E1, E2, and E3), Poisson's ratios (μ1, μ2, and μ3), and shear moduli (G12, G13, and G23). Among them, E1, E2, and E3, respectively, represent the elastic moduli of Chinese fir in the longitudinal direction, L; the radial direction across the grain, R; and the tangential direction across the grain, T. G12, G13, and G23, respectively, represent the shear moduli of the radial section, LR; the tangential section, LT; and the cross-section, RT. νij represents the Poisson's ratio, which refers to the relevant discussion in the "Wood Structure Design Manual", and the stress–strain relationship in the elastic stage of wood is expressed by the following matrix [29]:

$$\begin{aligned}
&D_{1111} = E_1(1-\nu_{23}\nu_{23})\gamma, D_{2222} = E_2(1-\nu_{13}\nu_{31})\gamma, D_{3333} = E_3(1-\nu_{12}\nu_{21})\gamma \\
&D_{1122} = E_1(\nu_{21}+\nu_{31}\nu_{23})\gamma = E_1(\nu_{12}+\nu_{32}\nu_{13})\gamma \\
&D_{1133} = E_3(\nu 13+\nu_{12}\nu_{23})\gamma = E_1(\nu_{31}+\nu_{21}\nu_{32})\gamma \\
&D_{2233} = E_2(\nu_{32}+\nu_{12}\nu_{31})\gamma = E_3(\nu_{23}+\nu_{21}\nu_{13})\gamma \\
&D_{1212} = 2G_{12}, D_{1313} = 2G_{13}, D_{2323} = 2G_{23} \\
&\gamma = 1/(1-\nu_{12}\nu_{21}-\nu_{13}\nu_{31}-\nu_{23}\nu_{32}-2\nu_{21}\nu_{32}\nu_{13}) \\
&\varepsilon_{12} = \gamma_{12}/2, \varepsilon_{13} = \gamma_{13}/2, \varepsilon_{23} = \gamma_{23}/2
\end{aligned} \tag{1}$$

The Chinese fir material used in this paper is from the same batch as that used in the material property test. The determination of the specimen size and the formulation of the test method are all carried out with reference to "Test Methods for Physical and Mechanical Properties of Clear Small-Sized Wood Specimens-Part 1" [30]. The main test contents include the air-dry density of the Chinese fir material, the strengthening degree of the material (including tensile strength along the grain, compressive strength along the grain, and compressive strength in the transverse (radial) and transverse (tangential) directions), the elastic constants of the material (including elastic moduli in tension and compression along the grain, elastic moduli in compression in the transverse (radial) and transverse (tangential) directions, and elastic modulus in bending), and the Poisson's ratios

of the material (including Poisson's ratio along the grain, Poisson's ratio in the transverse (radial) and transverse (tangential) directions) [31]. The specific parameters are as follows:

(1) The specific values of the material properties of wood in the elastic stage are shown in Table 3 below.

Table 3. Values of material properties of wood in the elastic stage.

E_1/MPa	E_2/MPa	E_3/MPa	μ_{12}	μ_{13}	μ_{23}	G_{12}/MPa	G_{13}/MPa	G_{23}/MPa
10,969.7	250	242.7	0.54763	0.46125	0.409	857.25	685	205

(2) The Hill yield criterion is used to determine the yield stress in different directions during the plastic phase [32]. σ_0 represents the reference value of the yield strength (in this paper, the compressive strength along the grain is selected), σ_{ij} represents the yield stress value of the material in each direction, and R_{11}, R_{22}, R_{33}, R_{12}, R_{13}, and R_{23} represent the ratios of the yield strengths in each direction. The yield strengths and yield strength coefficients in each direction of wood in the plastic stage are shown in Table 4.

Table 4. Yield strength values of wood in each direction.

Yield Strength (MPa)	σ_{11}	σ_{22}	σ_{33}	σ_{12}	σ_{13}	σ_{23}	σ_0
	25	1.5	1.5	2.01	2.01	2.01	25
Yield Strength Coefficient	R11	R22	R33	R12	R13	R23	
	1	0.06	0.06	0.12	0.12	0.12	

Steel is an elastoplastic material, as shown in Figure 14, and a linear strengthening model is selected. The elastic modulus is 210,000 MPa, and the Poisson's ratio is 0.3. The steel of the sleeve is Q235, so the yield stress is taken as 375 MPa. The bolt is a high-strength bolt of grade 10.9 M12, and the yield stress is taken as 900 MPa.

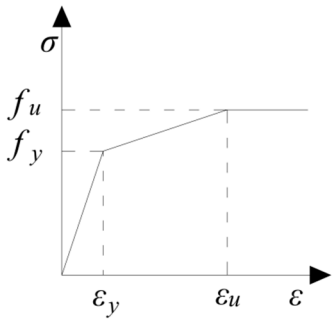

Figure 14. Constitutive model of steel.

4.2. Mesh Generation and Element Selection

The rationality of mesh generation and element selection is crucial for the accuracy of calculation and analysis results. Therefore, all structures in this paper are constructed using eight-node hexahedral linear shrinkage three-dimensional solid elements C3D8R. Their advantage is that when the mesh is distorted, the calculation accuracy will not be overly affected, and the structure is not prone to shear locking under the action of bending moment [33].

During the process of model construction, ABAQUS software provides three mesh generation techniques, including free mesh, swept mesh, and structured mesh. Among them, the unit mesh generated by the structured mesh is uniform and fine, and the unit

distortion is small, which is more in line with the calculation concept of this chapter. In ABAQUS finite element software, the master surface and the slave surface must be defined when defining interactions, with the stiffer surface being chosen as the master surface and the less stiff surface being chosen as the slave surface. If the stiffness of the two contact surfaces is similar, the surface with the coarser mesh should be chosen as the master surface. When simulating the test joints, there is mutual load-bearing friction between the wooden beams, wooden columns, and steel sleeves, which required surface-to-surface contact. At the same time, to ensure better convergence of the model and the correctness of the results, the mesh size of each component had to be adjusted multiple times. The main models in this paper are all meshed using the structured mesh generation method as shown in Figure 15. Considering factors such as calculation and analysis time and contact relationships, after multiple mesh attempts before the formal analysis, the calculation time is shortened as much as possible while ensuring the calculation accuracy. Finally, the mesh size of the column is determined to be 12 mm, the mesh size of the beam is 10 mm, the mesh size of the sleeve is 15 mm, the stiffener is 3 mm, and the bolt is 5 mm. Because the deformation of the bolt hole is relatively complex, it needs to be meshed separately to ensure the mesh quality of other regions. Using a global meshing approach to divide the grid would result in poor mesh quality around the bolt holes and make the model difficult to converge due to the complex stress near the bolt holes. Therefore, it is necessary to use an edge-based meshing method, where the "number of seeds" is set to three for meshing. The mesh quality will be poor when the number is too large, and the mesh will be too dense when the number is too small, which makes convergence difficult and analysis time-consuming. The unit division method is a swept hexahedral unit. By arranging mesh seeds in the local area and controlling the number of nodes to three, an excellent curved surface mesh can be obtained.

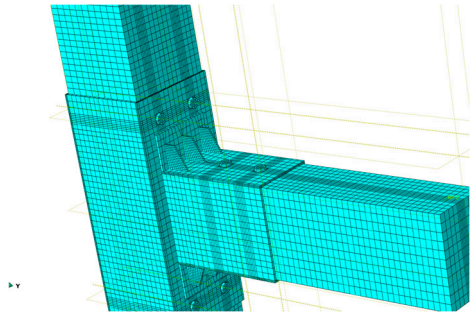

Figure 15. Schematic diagram of mesh generation.

4.3. Contact Settings

This model contains five contact forms, including the contact of wood at the tenon joint, the contact between the wooden structure and the sleeve, the contact between the bolt and the bolt hole, the contact between the stiffener and the sleeve, and the contact between the beam sleeve and the column sleeve. Three different contact definition methods are adopted.

Because there is contact between the tenon and mortise when simulating the test joint using ABAQUS, as well as between the steel sleeve and the beam–column, and due to the different surface roughness of wood and steel, the friction coefficients between wood and steel and between wood and wood are not the same. Therefore, it is necessary to set different friction coefficients. In the finite element simulation process of this model, all normal actions adopt the "Hard Contact" mode, and the tangential actions all adopt the "Penalty" function. According to the experimental research results of previous scholars [34,35], generally, the friction coefficient between wood and wood is between 0.2 and 0.6. In this paper, the

friction coefficient between wood and wood in each joint is taken as 0.3. The friction coefficient between wood and steel is approximately between 0.1 and 0.4. In this paper, the friction coefficient between wood and steel in each joint is taken as 0.25.

The surface of the tenon and mortise hole of the test specimen is relatively rough, and there is only a small gap. Therefore, in the J-1 joint, the friction coefficient between wood and wood is selected to be 0.3.

In the J-2 joint, a large amount of structural glue was evenly applied on the surface of the tenon and mortise hole to increase the friction coefficient. In this joint, the friction coefficient between wood and wood is set to 0.6. For the connection between the angle steel and wood, the friction coefficient between them is selected to be 0.3, and the connection between the self-tapping screw and wood is simplified as a surface-to-surface contact.

In the J-3 and J-4 joints, the interaction between the tenon and mortise hole is consistent with the model of the J-1 joint. In the test, the failure forms of the joints strengthened by the sleeve and bolt mainly include four types: the failure of the tenon, the failure at the lap joint between the wood and the sleeve, the failure at the stiffener, and the failure of the bolt hole. In this test, neither the bolt nor the sleeve slipped. To simplify the finite element model and shorten the calculation time, the contacts between the bolt and the bolt hole, the connection between the sleeves, and the contact between the stiffener and the sleeve are all set as "Tie" tied connections.

4.4. Boundary Conditions and Load Application System

All joint models adopt the same boundary conditions and load application mode as the test. The boundary positions are located at the top of the column, bottom of the column, and the upper loading surface of the beam.

When applying the boundary conditions of the column, to ensure that the column has no rigid body displacement and out-of-plane instability, the displacements in the X- and Z-directions and the angular displacement in the Y-direction need to be restricted at the upper and lower ends of the column, as shown in Figure 16. A reference point RP-1 is set at a distance of 70 mm from the top of the column at the upper end of the column. This reference point and the top surface of the column are defined as a distributed coupling constraint. On the one hand, the initial displacement boundary condition is defined at this point, and on the other hand, a 25 kN vertical load boundary is applied at this point to simulate the vertical load applied by the jack in the test. At the lower end of the column, as only the initial displacement boundary condition needs to be applied, there is no need to set a reference point, and the initial boundary condition can be directly defined on the lower surface of the column.

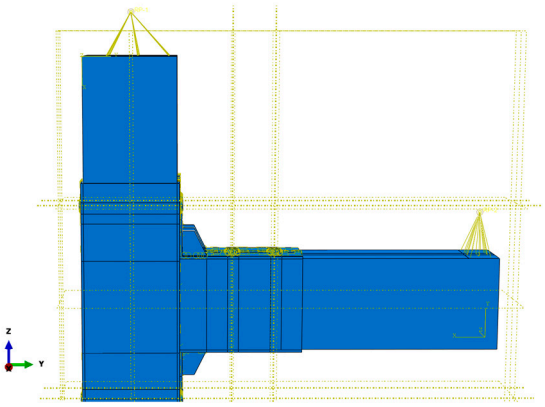

Figure 16. Distributed coupling constraints at the top and end of the column.

When applying the load at the beam end, it is necessary to strictly follow the test situation. A loading area is demarcated at a distance of 460 mm from the tenon at the beam end, and a reference point is set 70 mm directly above the center point of the loading area. The reference point and the upper surface of the loading area are defined as a distributed coupling constraint, and a displacement boundary is applied at this point. The specific boundary condition settings are shown in Table 5.

Table 5. Settings of each boundary condition in the joint.

Boundary Conditions	Boundary Location		Condition Settings
	Reference Point	Coupling Surface	
Load boundary	RP-1	Column top	A concentrated force in the Z-axis direction with a vertical load of 25 kN
Displacement boundary	RP-1	Column top	Constraints on displacements U1 and U3 and rotation UR2
	None	Column bottom	Constraints on displacements U1 and U3 and rotation UR2
	RP-2	Loading surface at the beam end	Application of a predetermined displacement load in the Z-direction

Note: U1, U3, and UR2, represent the displacements in the X-directions, Z-directions and the angular displacements around the Y-directions.

The entire model is divided into three load steps, namely the initial load step (step-initial), the first load step (step-1), and the second load step (step-2), so that the load can be increasingly introduced into the model in stages and so that the model can gradually and smoothly enter the stressed state.

- Initial load step (step-initial):
  - First, add contact relationships to each component in the model;
  - Second, set the initial displacement boundary conditions at the upper and lower ends of the column, which is consistent with the one-way hinged support that fixes the upper and lower ends of the column in the test.
- First load step (step-1): Add the corresponding load boundary at the top of the column. The axial force in the Z-direction is 25 kN, which is the same as the fixed load applied by the jack at the top of the column in the test.
- Second load step (step-2): Apply the full-range displacement load at the beam end. During the calculation process, the maximum displacement is set to 100 mm. In addition, the NIgeom switch in ABAQUS is set to on to consider geometric nonlinearity.

4.5. Comparison Between Finite Element Calculation Results and Experimental Calculation Results

Figure 17 shows the comparison of the moment–rotation (M–θ) curves between the experimental results and the finite element results of each specimen. The finite element values are represented by the red line, and the experimental values are represented by the black line.

By comparing and analyzing the M–θ curves of the experimental results and the finite element calculation results, it is found that the trends of the two are basically consistent, both showing the state of elastic straight-line rising stage → elastoplastic curve stable stage → strengthening curve rising stage → bearing capacity curve descending stage.

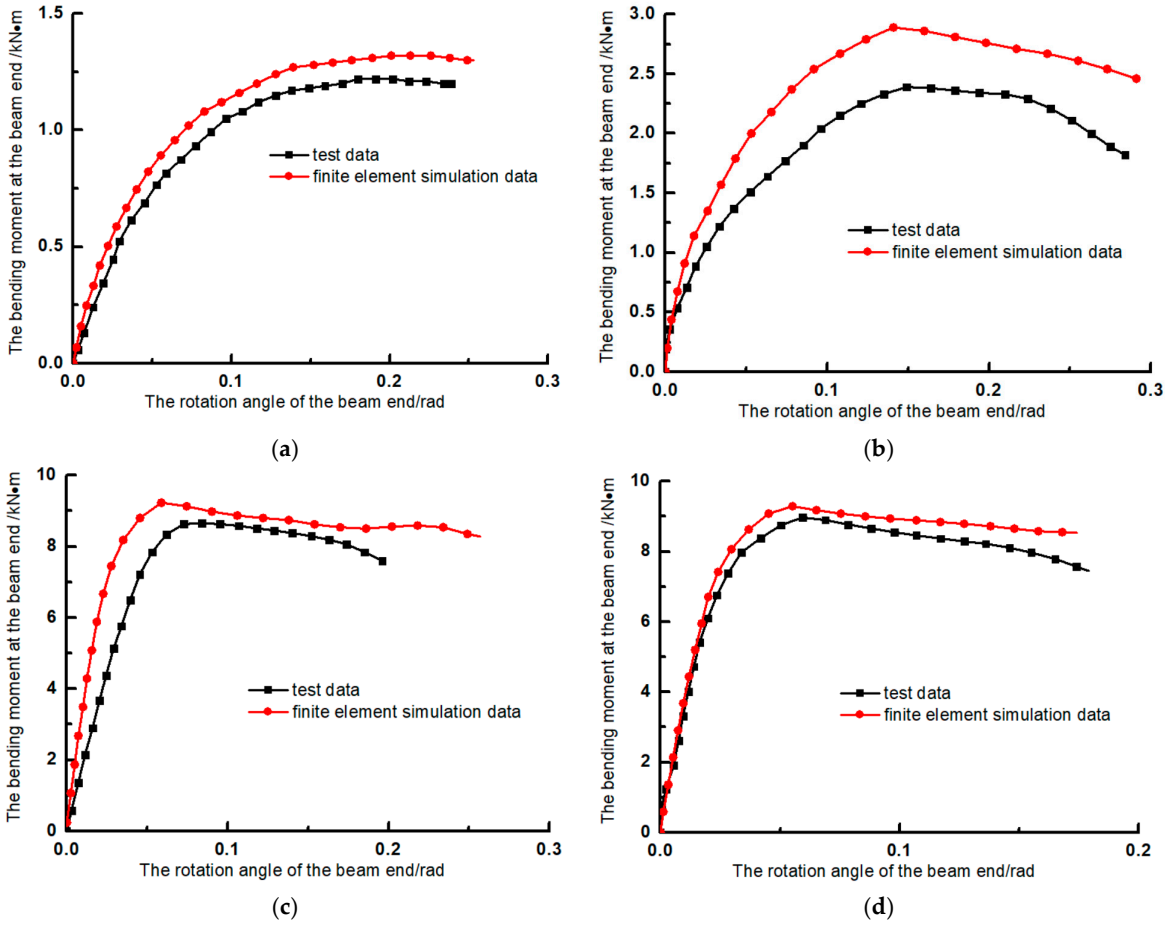

Figure 17. Comparison between finite element analysis results and experimental results. (**a**) J-1, (**b**) J-2, (**c**) J-3, and (**d**) J-4.

4.6. Analysis of Finite Element Stress Nephogram

4.6.1. J-1 Joint

The beam rotates in the longitudinal direction of the column, as shown in Figure 18. During the loading process, the upper flange of the tenon is extruded and deformed, the lower flange is stretched and deformed, and the upper and lower flanges of the mortise hole are both extruded and deformed. Except for the joint area, the stress on the beam and column is low, and the failure mode of this joint is tenon pulling-out failure.

During the initial loading stage, the stress on the upper and lower flanges of the tenon increases, and the deformation amount also gradually increases. As the load continues to be applied, the stress on the surface of the lower flange of the tenon reaches 25 MPa, and it first enters the yielding stage, as shown in Figure 18a. With the increase in the rotation angle, the plastic region of the tenon gradually becomes larger, and at this time, the upper flange also enters the plastic yielding stage, and extrusion deformation occurs, as illustrated in Figure 18b. With the continuous increase in the external load, when the mortise opening enters the plastic yielding stage, the bearing capacity of the joint enters a slow descending stage, the extrusion area gradually decreases, and the tenon pulling-out amount continues to increase, as plotted in Figure 18c, until the tenon completely disengages from the mortise hole, and the bearing capacity of the joint suddenly drops to zero. By comparing and analyzing the experimental phenomenon and finite element analysis results, it can be found that during the loading process, the joint mainly resists the bending moment deformation by the upper and lower surfaces of the mortise hole and the upper and lower flanges of the

tenon, and the stress on the side surfaces of the tenon and mortise hole is small and can be ignored.

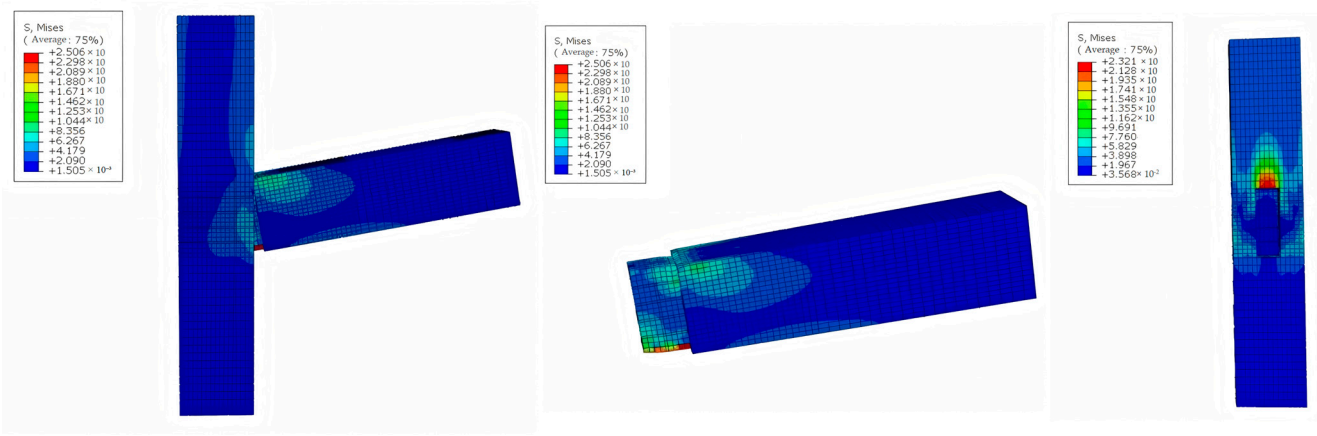

(**a**) (**b**) (**c**)

Figure 18. Stress nephogram of J-1 joint (unit: MPa). (**a**) Overall failure stress nephogram of the joint, (**b**) failure stress nephogram of the beam end, and (**c**) failure stress nephogram of the mortise hole at the column end.

4.6.2. J-2 Joint

As shown in Figure 19a, the stress at the location where the self-tapping screw is connected is the highest, followed by the upper and lower flanges of the tenon and the upper and lower surfaces of the mortise hole, but there is no obvious stress change at the angle steel.

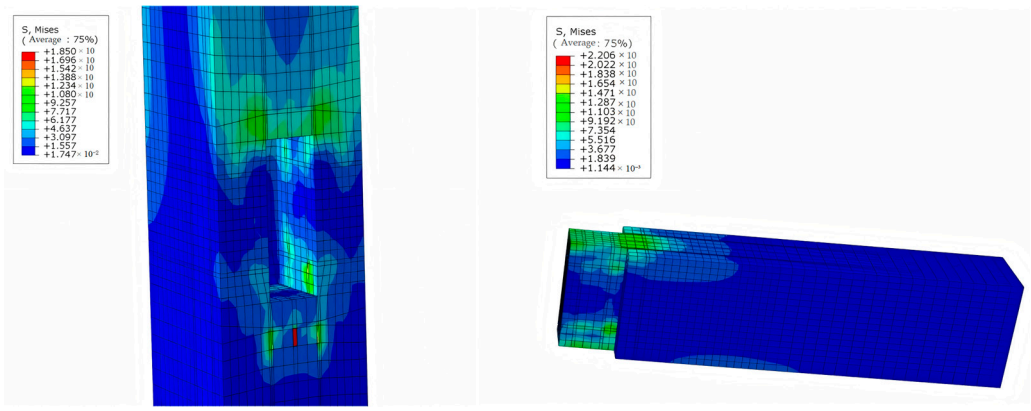

(**a**) (**b**)

Figure 19. Stress nephogram of the J-2 joint (unit: MPa). (**a**) Failure stress nephogram of the column end; (**b**) failure nephogram of the beam end.

As shown in Figure 19b, during the initial stage of the load, the stress at the side wall and the upper and lower surface self-tapping screw connection in the joint area gradually increases. During this process, the self-tapping screw has not yet come out, and the angle steel has no sliding trend. However, when the stress value reaches 25 MPa, it enters the plastic stage; at this time, the self-tapping screw begins to come out, the angle steel begins to slide, and the joint shows the tenon pulling-out phenomenon, and the corresponding rotation angle also gradually increases. As shown in Figure 18c, the lower flange of the tenon is gradually damaged and shows obvious tensile deformation with the increase in the joint rotation angle and, at the same time, with the gradual expansion of the plastic region, and the upper flange of the tenon also shows compressive deformation. Finally,

the mortise hole enters the plastic state, the extrusion area gradually shrinks, the tenon pulling-out amount gradually increases until the tenon disengages from the mortise hole and, at this time, the joint load drops to zero.

4.6.3. J-3 Joint

As shown in Figure 20a, the beam rotates in the longitudinal direction of the column. During the loading process, the upper flange at the lap joint of the beam and the beam sleeve is fractured, and the lower flange maintains tensile deformation. The beam sleeve is bulged and inclined, and the stiffener is extruded and bulged. The failure mode of this joint is the fracture failure of the beam.

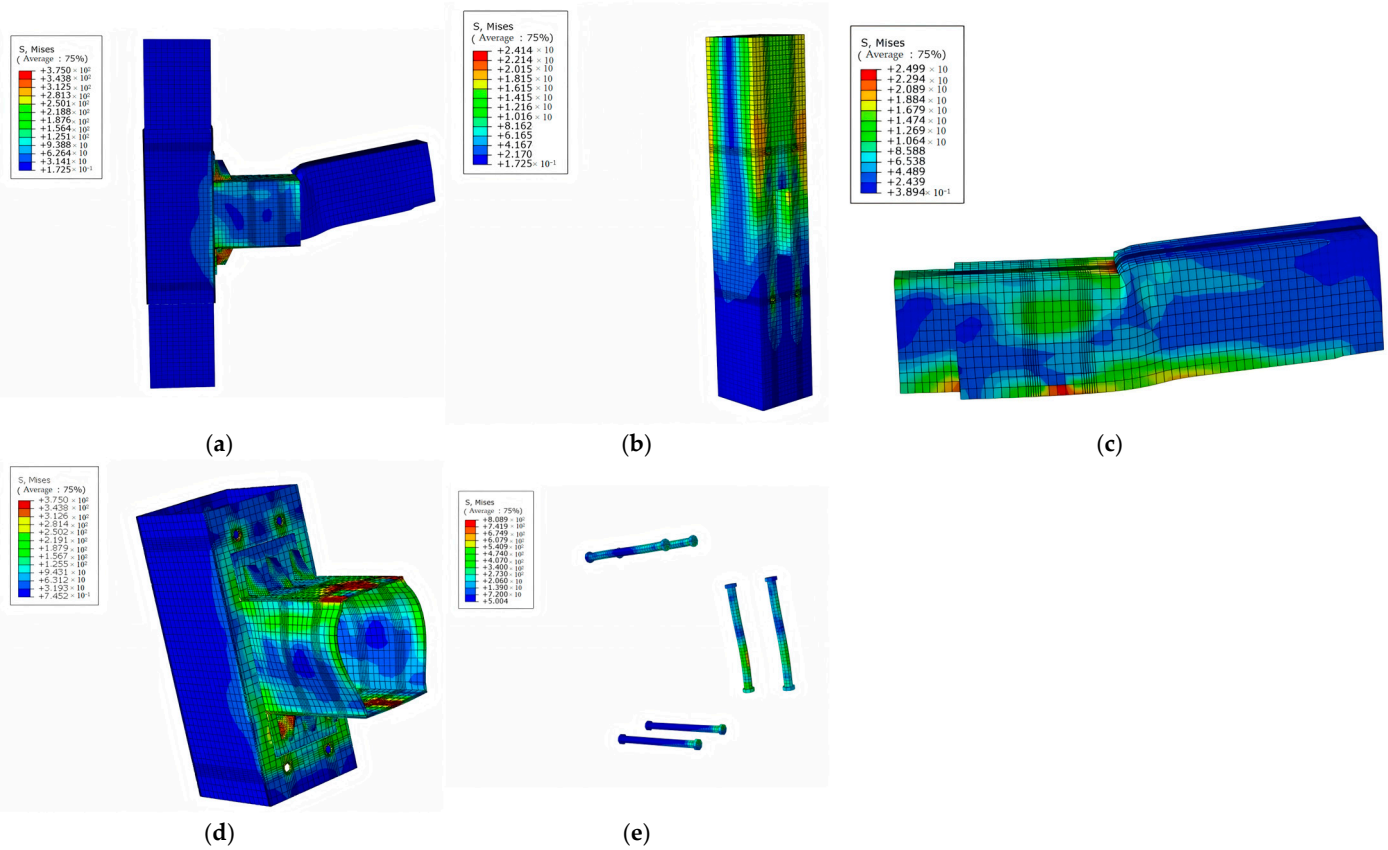

Figure 20. Stress nephogram of the J-3 joint (unit: MPa). (**a**) Stress nephogram of overall joint failure, (**b**) stress nephogram of column end failure, (**c**) stress nephogram of beam end failure, (**d**) failure stress nephogram of the sleeve, and (**e**) failure stress nephogram of the bolt.

During the initial loading stage, the beam is constrained by the beam sleeve and bolts, and the bolt hole area on the beam and the upper flange at the lap joint with the sleeve are compressed and deformed, and the deformation degree increases with the increase in the rotation angle. The area around the bolt hole on the beam yields first and undergoes plastic deformation with the load continuously increasing, which is basically consistent with the experimental observation. The plastic range gradually expands with the continuous increase in the rotation angle, and the upper and lower flanges at the lap joint of the beam and the sleeve enter the plastic yielding state; the upper flange is extruded and deformed, and the lower flange is stretched and deformed. At this time, the entire joint is restrained by the sleeve, the upper flange at the lap joint of the beam and the sleeve is gradually crushed by extrusion, the beam sleeve is slowly deformed, and its upper and side surfaces bulge. The joint rotation angle continues to increase until the beam fractures and the bearing capacity drops to zero. The loading and deformation process of this joint model is basically

consistent with the experimental data, and the deformation diagram of the beam is slightly different from the actual observation. The reason for the fracture on the upper surface of the beam in the experiment is that the overall stability of the weld is poor during the factory processing process.

It can be seen from the simulation nephogram in Figure 20b that the upper end of the column bears a large bending moment, which is consistent with the experimental observation. The tenon and mortise hole do not have serious stress changes and deformations during the entire loading process, and the sleeve plays a protective role in the core area of the joint to a certain extent, as plotted in Figure 20c. The stiffener reaches the yield strength at the mortise–tenon connection, enters the plastic stage, and undergoes plastic deformation, thereby improving the flexural performance of the entire joint, as illustrated in Figure 20d. The stress of the bolt connection is low, and no obvious damage occurs, as shown in Figure 20e.

4.6.4. J-4 Joint

As shown in Figure 21a, the failure mode of this joint is the same as that of the J-3 joint, both of which are the fracture of the beam end, resulting in the loss of bearing capacity. Compared with the J-3 joint, the difference is that the stiffener in the J-4 joint does not show significant deformation, no obvious bending is observed in the 6 mm steel plates on the upper and lower surfaces of the beam sleeve, and the degree and area of damage to the wooden beam are larger, as shown in Figure 21b,c. Therefore, it indicates that appropriately increasing the thickness of the upper and lower surfaces can improve the bearing capacity of the joint to a certain extent, but if the thickness is too thick, the wooden beam and the sleeve cannot work together.

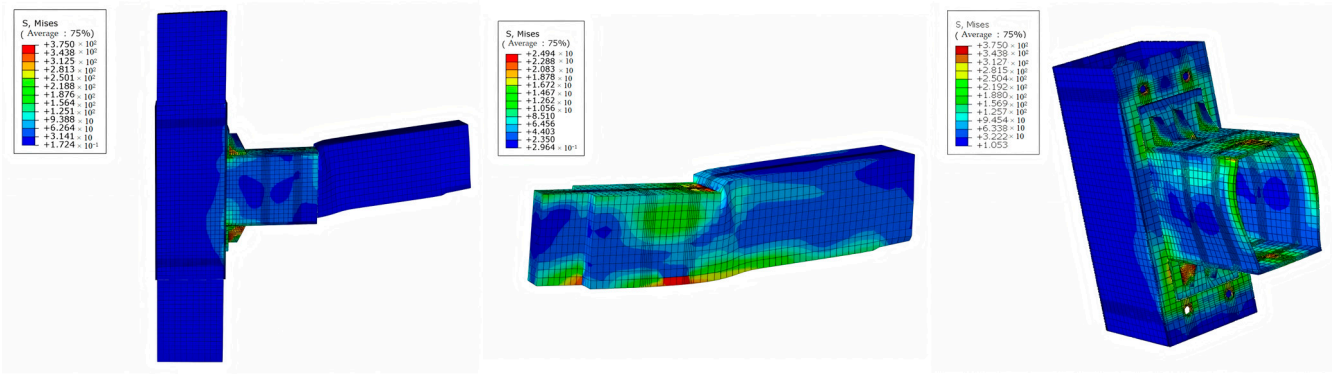

(**a**) (**b**) (**c**)

Figure 21. Stress nephogram of the J-4 joint (unit: MPa). (**a**) Overall failure stress nephogram of the joint, (**b**) failure stress nephogram of the beam end, and (**c**) failure stress nephogram of the sleeve.

5. Conclusions

A set of pure timber joints and three sets of reinforced joints underwent monotonic loading tests and numerical simulations, from which the following conclusions were drawn:

(1) In the monotonic loading tests, the joints without steel sleeve reinforcement exhibited compression deformation at both the mortise hole and the upper surface of the tenon under the action of the bending moment. Additionally, a tenon pulling phenomenon occurred on the lower surface of the tenon. Ultimately, the entire joint suffered from tenon pulling failure, leading to a loss of bearing capacity for the specimen. Compared with the joints without steel sleeve reinforcement, the load-bearing capacity and initial stiffness of the joints with steel sleeve reinforcement are significantly improved. The failure mode is characterized by the fracture at the edges of the steel plate and the

tearing deformation of the wooden beam, while the wooden column and the column sleeve remain intact and undamaged. Designing new types of reinforced joints can provide a variety of reinforcement methods to meet different structural requirements and economic benefits.

(2) The M–θ curves of the specimens show a downward trend. The stiffness of all joints decreases with the increase in joint rotation angle, and the joints without steel sleeve reinforcement have lower initial stiffness and a faster rate of degradation, which indicates poorer seismic resistance for the joint. The joints reinforced with steel sleeves have a high initial stiffness. Although the rate of degradation slows down gradually in the later stages of loading, it still tends to stabilize slowly, which demonstrates good seismic performance for the joint. The maximum value of the tenon pulling for the joint does not change significantly due to the factors of angle steel, self-tapping screws, or structural adhesive, while the tenon pulling amount in the sleeve-reinforced joints is minimal, which indicates that the tenon pulling failure is effectively prevented by the steel sleeves.

(3) In numerical simulations, the areas with high stress in joints without sleeve reinforcement are primarily located at the upper and lower ends of the tenon. The compressive stress at both the upper and lower edges of the tenon is mainly distributed along the grain direction of the beam. The stress becomes more pronounced as the distance to the variable cross-section decreases. The stress on the column sleeve of joints reinforced with steel sleeves and bolts is relatively low. Meanwhile, the areas with greater strain in the beam sleeve are mainly concentrated on the side with the welded stiffeners and its surroundings. Additionally, the strain around the bolt holes is quite noticeable.

Author Contributions: Conceptualization, Z.W. and J.S.; methodology, Z.W. and J.S.; software, Z.G. and J.S.; validation, Z.W. and J.S.; formal analysis, Z.W. and J.S.; investigation, Z.W. and J.S.; resources, Z.W. and J.S.; data curation, W.Y.; writing—original draft preparation, Z.G.; writing—review and editing, D.L. and J.S.; visualization, J.S.; supervision, Z.W.; project administration, Z.W.; funding acquisition, Z.W. All authors have read and agreed to the published version of the manuscript.

Funding: This research was funded by the Integrated Construction Project of Disciplines, Majors and Platform Teams during the "14th Five-Year Plan" of Kaili University (YTH-PT202403), the Special Research Project for Doctoral Development of Kaili University (Grant No. BSFZ202207), the Science and Technology Program of Qiandongnan Prefecture (Grant No. Qiandongnan Kehe Jzi [2023]03), and the National Natural Science Foundation of China (Grant No. 12462010).

Data Availability Statement: The original contributions presented in this study are included in the article. Further inquiries can be directed to the corresponding author.

Conflicts of Interest: The authors declare no conflicts of interest.

References

1. Fa, G.; Wang, Q. Experimental study on seismic performance of mortise-tenon joints strengthened with BFRP. *Build. Struct.* **2012**, *42*, 152–156.
2. Zhou, Q.; Yan, W.; Zhou, H.; Zhang, Y. Seismic test of ancient building mortise-tenon joints strengthened with steel components. *J. Appl. Basic Eng. Sci.* **2012**, *20*, 1063–1071.
3. Xu, M.; Qiu, H.; Chun, Q. Calculation of bearing capacity of mortise-tenon joints of ancient wooden structures strengthened with carbon fiber. *Earthq. Resist. Eng. Retrofit.* **2013**, *35*, 121–124.
4. Chang, W.; Hsu, M.; Komatsu, K. Rotational performance of traditional Nuki joints with gap I: Theory and verification. *J. Wood Sci.* **2006**, *52*, 58–62. [CrossRef]
5. Chang, W.; Hsu, M. Rotational performance of traditional Nuki joints with gap II:the behavior of butted Nuki joint and its comparison with continuous Nuki joint. *J. Wood Sci.* **2007**, *53*, 401–407. [CrossRef]

6. Shao, J.; Wang, K.; Kaewunruen, S.; Cai, W.; Wang, Z. Experimental Investigations into Earthquake Resistance of Steel Frame Retrofitted by Low-Yield-Point Steel Energy Absorbers. *Appl. Sci.* **2019**, *9*, 3299. [CrossRef]
7. Xu, T.; Shao, J.; Zhang, J.; Kaewunruen, S. Experimental Performance Evaluation of Multi-Storey Steel Plate Shear Walls Designed by Different Methods. *Int. J. Civ. Eng.* **2019**, *17*, 1145–1154. [CrossRef]
8. Wang, Z.; Shao, J. Study on Quasi-Static Axial Compression Performance and Energy Absorption of aluminum Foam-Filled Steel Tubes. *Materials* **2023**, *16*, 4485. [CrossRef] [PubMed]
9. Liu, K.; Shao, J.; Tang, B.; Wu, Q.; Wang, Z. Seismic Performance of Low-Yield-Point Steel Plate Shear Walls Under Horizontal Cyclic Load. *Iran. J. Sci. Technol. Trans. Civ. Eng.* **2022**, *16*, 3739–3752. [CrossRef]
10. Liu, Q.; Shao, J.; Tang, B.; Wang, Z. Experimental Investigation into Failure Modes of Low-Yield-Point Steel Plate Shear Walls. *Appl. Sci.* **2022**, *12*, 5632. [CrossRef]
11. Wang, T.; Shao, J.; Zhao, C.; Liu, W.; Wang, Z. Shaking Table Test for Evaluating the Seismic Performance of Steel Frame Retrofitted by Buckling-Restrained Braces. *Shock. Vib.* **2021**, *2021*, 6654201. [CrossRef]
12. Wang, T.; Shao, J.; Xu, T.; Wang, Z. Study on Axial Compression Properties of Aluminum Foam-flled Steel Tube Members After High Temperature. *Iran. J. Sci. Technol. Trans. Civ. Eng.* **2021**, *46*, 883–900.
13. Chen, C.; Qiu, H.; Bao, Y.; Hao, X. Experimental study on flexural performance of asymmetric mortise-tenon joints under positive and negative bending. *J. Southeast Univ. (Nat. Sci. Ed.)* **2014**, *44*, 1224–1229.
14. Yang, H.F.; Ling, Z.B.; Liu, W.Q.; Ren, X.; Lu, W.D. Experimental study on ductile flexural joints of glued laminated timber beams and columns under monotonic and low-cycle repeated loads. *J. Build. Struct.* **2015**, *69*, 131–138.
15. Tannert, T. Improved performance of reinforced rounded dovetail joints. *Constr. Build. Mater.* **2016**, *118*, 262–267. [CrossRef]
16. Crayssac, E.; Song, X.; Wu, Y.; Li, K. Lateral performance of mortise-tenon jointed traditional timber frames with wood panel infill. *Eng. Struct.* **2018**, *161*, 223–230. [CrossRef]
17. Rad, A.R.; Burton, H.; Weinand, Y. Performance assessment of through-tenon timber joints under tension loads. *Constr. Build. Mater.* **2019**, *207*, 706–721.
18. Panoutsopoulou, L.; Mouzakis, C. Experimental investigation of the behavior of traditional timber mortise-tenon T-joints under monotonic and cyclic loading. *Constr. Build. Mater.* **2022**, *348*, 128655. [CrossRef]
19. Wang, M.; Song, X.; Gu, X.; Zhang, Y.; Luo, L. Research on rotational performance of bolt-steel filler plate joints of glued laminated timber beams and columns. *J. Build. Struct.* **2014**, *35*, 141–150.
20. Sun, H.; Lu, W.; Zhao, K.; Fan, N. Calculation of flexural bearing capacity of bolted joints of glued laminated timber beams and columns enhanced by self-tapping screws. *Struct. Eng.* **2015**, *31*, 46–50.
21. Luo, E. Research on Mechanical Properties of Bolted Joints with Built-In Steel Plates in Wooden Reticulated Shells. Master's Thesis, Harbin Institute of Technology, Harbin, China, 2015; pp. 70–71.
22. Zhou, T.; Guan, Z. A new approach to obtain flat nail embedding strength of double-sided nail plate joints. *Constr. Build. Mater.* **2011**, *25*, 598–607. [CrossRef]
23. Bader, T.K.; Schweigler, M.; Hochreiner, G.; Serrano, E.; Enquist, B.; Dorn, M. Dowel deformations in multi-dowel LVL-connections under moment loading. *Wood Mater. Sci. Eng.* **2015**, *10*, 216–231. [CrossRef]
24. Masaeli, M.; Karampour, H.; Gilbert, B.P.; Talebian, N.; Behnia, A. Numerical assessment of the interaction between shear and moment actions in LVL bolted connections. *J. Build. Eng.* **2022**, *55*, 104695. [CrossRef]
25. Li, J. *Yingzao Fashi*; The Commercial Press: Shanghai, China, 1950.
26. *GB 50005-2003*; Code for Design of Timber Structures. Standardization Administration of China: Beijing, China, 2003.
27. Wang, W. Research on Mechanical Properties of Mortise-Tenon Joints of Ancient Wooden Structures After Reinforcement. Master's Thesis, Southeast University, Nanjing, China, 2017.
28. Xu, D.; Xue, J.; Qi, L.; Chen, J.; Xu, Y. Research on seismic performance of hook mortise joints of column-and-tie timber structures. *J. Build. Struct.* **2024**, *45*, 187–196.
29. Cao, L. Simulation Study on Seismic Performance of Single- and Double-Span Timber Structures. Master's Thesis, Taiyuan University of Technology, Taiyuan, China, 2017.
30. Wang, T. Research on Mechanical Properties and Fire Resistance of Joints of Ethnic Timber Structures in Southeast Guizhou. Master's Thesis, Jiangsu University of Science and Technology, Zhenjiang, China, 2021.
31. *GB/T 1927.1-2021*; Test Methods for Physical and Mechanical Properties of Clear Small-Sized Wood Specimens—Part 1: Collection of Test Materials. Standardization Administration of China: Beijing, China, 2021.
32. Wang, Z.; Shi, A.; Wang, T.; Shao, J. Research on the Physical and Mechanical Properties of Chinese Fir in Southeast Guizhou. *Fujian Archit. Constr.* **2020**, *06*, 87–91.
33. Xue, J.; Liang, X.; Song, D.; Wu, C. Experimental Research and Finite Element Analysis on the Eccentric Compression Performance of Bracket Sets of the Capital. *J. Build. Struct.* **2022**, *43*, 199–209.

34. Li, Y.; Cheng, X.; An, Y.; Yang, X.; Lu, G.; Liu, J. Experimental and Finite Element Analysis on the Seismic Performance of the Cantilever Section of a New Stepped Joint. *J. Harbin Inst. Technol.* **2024**. Available online: https://link.cnki.net/urlid/23.1235.T.20240201.1230.002 (accessed on 28 December 2024).
35. Gan, S. Experimental Research and Engineering Demonstration on the Seismic Performance of Traditional Timber Structure Mortise-Tenon Joints Strengthened with Viscoelastic Dampers. Master's Thesis, Kunming University of Science and Technology, Kunming, Yunnan, 2023.